www.sciencemag.org/content/353/6304/1117/suppl/DC1

Supplementary Materials for

Synaptic mechanisms of pattern completion in the hippocampal CA3 network

Segundo Jose Guzman, Alois Schlögl, Michael Frotscher, Peter Jonas*

*Corresponding author. E-mail: peter.jonas@ist.ac.at

Published 9 September 2016, *Science* **353**, 1117 (2016)
DOI: 10.1126/science.aaf1836

This PDF file includes:

MATERIALS AND METHODS

EXPERIMENTAL PROCEDURES

Slice preparation and octuple recording

Thick transverse hippocampal slices (400 µm) were cut from left or right brain hemispheres of 15- to 31-day-old Wistar rats of either sex using a VT 1200 vibratome. Animals were kept in an oxygenated chamber for 30 min, lightly anaesthetized with isoflurane (0.4% (v / v) added to the chamber volume at a flow rate of 2–3 ml min^{-1}), and subsequently sacrificed by decapitation. Experiments were performed in strict accordance with institutional, national, and European guidelines for animal experimentation and were approved by the Bundesministerium für Wissenschaft, Forschung und Wirtschaft (A. Haslinger, Vienna). Hemispheres were mounted with "magic cut" angles of α close to 0 and β close to –5° (*48*), and were oriented such that the cutting blade advanced from basal to apical dendrites of CA3b pyramidal neurons. Parasagittal and frontal slice orientations were also tested, but resulted in reduced slice quality.

Patch pipettes were pulled from thick-walled borosilicate glass tubing (2 mm outer diameter, 0.5 mm wall thickness); when filled with intracellular solution, the resistance was 1.6–5 MΩ. Pipettes were positioned manually with eight LN mini 25 micromanipulators under visual control provided by infrared differential interference contrast (IR-DIC) videomicroscopy. Targeted cell bodies were located ~20–100 µm from the surface of the slice. CA3 pyramidal neurons were identified on the basis of morphological appearance in the videoimage and the action potential phenotype upon sustained current injection, with average firing frequencies of < 20 Hz during 1-s current pulses. Neurons with resting potentials more positive than –60 mV were discarded. The recording temperature was either ~22°C (range: 19–24°C, room temperature), or ~34°C (33–36°C, near-physiological temperature), as indicated. All recorded neurons were located in the CA3b subfield, a subregion with extensive recurrent collaterals (*35, 36*).

Electrical signals were recorded using either four Multiclamp 700B amplifiers or a combination of two Multiclamp 700B and four Axopatch 200B

amplifiers. Signals were low-pass filtered with built-in Bessel filters at 5 or 6 kHz and digitized at 20 kHz with a CED 1401 power3 AD/DA converter connected to a personal computer. Pulse generation and data acquisition were performed using Signal 6.0 and custom-made stimulation–acquisition protocols. The presynaptic neuron was held in the current-clamp mode and stimulated with a repetition interval of 10–20 s, unless differently specified. Action potentials were elicited by brief current pulses (duration 2–5 ms, amplitude 1–2 nA). The postsynaptic cells were held in either current- or voltage-clamp mode. For current-clamp recording, pipette capacitance and series resistance were compensated, and compensation was readjusted during the experiment when necessary. For voltage-clamp recording, series resistance was not compensated, but carefully monitored using 2-mV hyperpolarizing pulses following the evoked EPSC. For analysis of EPSC kinetics, series resistance was ≤ 10 MΩ (7.3 ± 0.3 MΩ). For multiple probability binomial analysis, series resistance was ≤ 15 MΩ and was constant within ≤ 20% of its initial value (see table S2).

To test for chemical synaptic connectivity, a presynaptic neuron under current-clamp conditions was stimulated with a train of 5 or 10 current pulses (duration 2–5 ms, amplitude 1–2 nA, frequency 10–50 Hz), while keeping all the other neurons in the voltage-clamp configuration at –70 mV (Fig. 1C). In total, 15–30 single traces were collected. A pair was judged to be monosynaptically connected if EPSCs were generated with a latency of < 3 ms at ~22°C and 1.6 ms at ~34°C, and had peak amplitudes of > 2.2–2.5 times the standard deviation of the preceding baseline. To test for electrical synapses, long hyperpolarizing current pulses (duration 250 ms, amplitude –50 pA) were applied to one neuron, and potential responses (outward currents) were examined in all other neurons. With this stimulation paradigm, electrical coupling could be unequivocally distinguished from capacitive coupling artifacts. In total, 15,930 pairs of neurons were tested for both chemical and electrical connectivity.

Labeling of pre- and postsynaptic neurons

Pre- and postsynaptic neurons were filled with biocytin (0.2%) during recording for > 1 hour. To restrict labeling to synaptically connected neurons, uncoupled cells were rapidly subjected to a nucleated patch “delabeling” procedure, by gently retracting the recording pipette while applying negative pressure (50–150 mbar; fig. S1). This minimized labeling of the perisomatic region of the unconnected cells, and completely prevented labeling of their subcellular processes (dendrites and axons).

After filling of pre- and postsynaptic neurons, pipettes were withdrawn from their somata, typically resulting in the formation of outside-out patches at the pipette tips. Slices were then fixed for 12–24 hours at 4°C in a 0.1 M phosphate buffer (PB) solution containing 2.5% paraformaldehyde (PFA), 1.25% glutaraldehyde (GA) and 15% (v/v) saturated picric acid solution. After fixation, slices were treated with hydrogen peroxide (1%, 10 min) to block endogenous peroxidases, and rinsed in PB several times. Membranes were permeabilized with 2% Triton X-100 in PB for 1 h. Slices were then transferred to a phosphate-buffered solution containing 1% avidin-biotinylated horseradish peroxidase complex (ABC) and 1% Triton X-100 for ~12 hr. Excess ABC was removed by several rinses in PB and the slices were developed with 0.036% 3,3'-diaminobenzidine tetrahydrochloride (DAB), 0.01% hydrogen peroxide, and a 0.006% $NiCl_2$ / 0.008% $CoCl_2$ mixture for intensification. Finally, slices were embedded in Mowiol.

Solutions

For dissection and maintenance of slices, a sucrose-containing solution composed of 87 mM NaCl, 25 mM $NaHCO_3$, 10 mM glucose, 75 mM sucrose, 2.5 mM KCl, 1.25 mM NaH_2PO_4, 0.5 mM $CaCl_2$, and 7 mM $MgCl_2$ was used. During recording, slices were superfused with a physiological extracellular solution containing 125 mM NaCl, 25 mM $NaHCO_3$, 25 mM glucose, 2.5 mM KCl, 1.25 mM NaH_2PO_4, 2 mM $CaCl_2$, 1 mM $MgCl_2$, equilibrated with 95% O_2 / 5% CO_2 gas mixture. The pipette solution contained 135 mM K-gluconate, 20 mM KCl, 0.1 mM EGTA, 2 mM $MgCl_2$, 4 mM Na_2ATP, 0.3 mM GTP, 10 mM HEPES, and 0.2% biocytin (pH

adjusted to 7.28 with KOH). In all experiments, 10 µM gabazine was added to the bath solution to block any contaminating disynaptic inhibitory events.

ANALYSIS

Analysis of unitary EPSPs and EPSCs

Unitary EPSPs and EPSCs were analyzed using C-Stimfit or Python-based scripts (*49*). The rise time was measured as the time interval between the points corresponding to 20 and 80% of the peak amplitude. The peak of the EPSP or EPSC was determined as the mean or maximum within a window of 1 or 2 ms duration, respectively, following the presynaptic action potential. The synaptic latency was determined as the time interval between the peak of the presynaptic action potential and the onset of the subsequent EPSP or EPSC; the onset point was determined from the intersection of a line through the 20 and 80% points with the baseline. The decay phase of the EPSPs or EPSCs was fit with a monoexponential function using a nonlinear least-squares fit algorithm. A trace was classified as a failure when the peak amplitude was less than three times the standard deviation of the preceding baseline. To quantify the multiple-pulse ratio, > 20 traces (including failures) were averaged. The amplitudes of the second and all subsequent EPSPs or EPSCs in the train were measured in average traces, setting the baseline directly before the onset of each synaptic event. To determine the number of inputs necessary to reach the firing threshold of a postsynaptic neuron, resting potentials were measured immediately after the whole-cell configuration was reached, and action potential voltage threshold was determined using depolarizing current ramps. Threshold was defined as the voltage at the point when the slope first exceeded a value of 20 V s^{-1} (Fig. 4, E and F).

To determine the number of functional release sites of a synaptic connection, EPSPs or EPSCs were recorded in different extracellular Ca^{2+} concentrations. The entire unbinned data set of peak amplitudes was analyzed by MP-BA (multiple probability binomial analysis) using maximum-likelihood fitting (*50*). Peak amplitude data were fit by a single release model, with free parameters q (quantal size; range: 3–25 pA or 0.03–2.5 mV), CV_q (coefficient of variation for

intra-site variability of q; range: 0.01–1.5), p_{R1} and p_{R2} (release probabilities in the two experimental conditions; range: 0.05–0.95), and different integer values of N (number of functional release sites; range: 1–10). One pair in which likelihood increased monotonically as a function of N was excluded from analysis. When the fit was not satisfactory, inter-site variability and variability in release probability were additionally tested. Unbinned data were analyzed by maximum-likelihood fitting.

Reconstruction, localization of synaptic contacts, and cable modeling

Neurons including soma, dendrites, and the entire axonal arborization were traced using a digital reconstruction system equipped with Neurolucida 9.0 reconstruction software (Microbrightfield), and 60 x / 1.4 numerical aperture (NA) and 100 x / 1.4 NA oil-immersion objectives. Dendrites were identified based on the high density of spines. Axons were unequivocally identified by the absence of spines and the larger branching angles. Putative synaptic contacts between functionally connected neurons were identified light-microscopically as crossings of an axon and a dendrite in the same focal plane, and the presence of an expansion (representing a putative bouton) on the presynaptic side. Only pairs in which the dendritic tree of the postsynaptic cell appeared largely intact were included in the analysis.

To estimate the true postsynaptic conductance at recurrent CA3–CA3 synapses, we simulated EPSCs in realistic cable models of CA3 pyramidal neurons. After reconstruction of dendritic and axonal morphology, Neurolucida data were imported into Neuron 7.3 (*52*). The spatial discretization was set according to the "d_lambda" rule with $d < 0.1\ \lambda_{100\ Hz}$. To ensure proper positioning of synapses, the spatial resolution for dendritic segments containing putative contacts was increased > 2 times. The integration time step was fixed to 10 μs.

The synapse was modeled as an AMPAR-mediated biexponential conductance. Latency, rise time constant, peak amplitude, and decay time constant were varied until the best fit to the measured EPSC was obtained (rise time constant range: 0.01–3 ms; peak amplitude range: 0.1–10 nS; decay time

constant range: 2–15 ms). Specific membrane capacitance was assumed as 1 μF cm^{-2}, specific membrane resistance as 164 kΩ cm^2, and intracellular resistivity as 194 Ω cm (*53*–55). The experimental value of series resistance for each experiment (≤ 10 MΩ) was realistically incorporated into the model.

Analysis of axon preservation in virtual slices

To assess the effects of slice preparation on connectivity, we performed a "virtual slicing" simulation, using previous reconstructions of three *in vivo* labeled CA3 pyramidal neurons (cells 51, 60a, and D256 imported from ModelDB; *35*, *51*, 56) (fig. S3). Neurons were shifted such that their somata were located in the center of the hippocampal formation (coordinates: x = 5600, y = 4200, and z = 2750 μm; *56*). Furthermore, cells were rotated so that dendritic sum vectors for apical and inverted basal dendrites were perpendicular to *stratum pyramidale–stratum radiatum* and *stratum oriens* boundaries.

To quantify the proportion of axons contained in a virtual slice section, sections of different orientation were simulated. Slice thickness was 400 μm, and the soma was located in the center of the section, unless differently specified. For each section, the cumulative length of preserved axon segments and the volume of the CA3 pyramidal neuron layer were computed. To determine whether an axon segment was located inside or outside the virtual slice section, Euclidian distance of the segment from the surface plane was calculated as $\vec{a} \cdot \vec{n}$, where $\vec{a}$ = (x_i, y_i, z_i), x_i, y_i, and z_i represent axon segment coordinates, and $\vec{n}$ is a normal unit vector perpendicular to the surface. This analysis revealed that the cumulative length of the axon contained in the virtual slice section was substantially reduced in comparison to the *in vivo* situation (fig. S3D). However, the volume of the CA3 pyramidal neuron layer contained in the section was reduced in parallel (fig. S3E), consistent with the idea that the average connectivity in the slice was relatively unchanged.

To quantify the axon connection factor in a given virtual slice section, i.e. the fraction of axon segments connected to the soma over the sum of all segments, axon segments inside a section were labeled as 1, and segments outside the

section as 0. For each axon segment, recursive backtracing to the soma was performed, and connectivity was computed as the product of all labels along the path. To mimic the experimental configuration, connectivity analysis was restricted to a 600-µm radius around the soma. The calculated axonal connection factor was ~40% for 400-µm-thick sections (fig. S3F), and decreased substantially as the thickness of the sections was reduced or the soma was shifted from the center to the surface of the section (fig. S3G). Thus, thick slices and deep recordings, as used in our experiments, better maintained connectivity. Based on these results, total connectivity was predicted as fraction of preserved axon length / fraction of preserved pyramidal cell volume x axon connection factor. This analysis suggested that transverse slices showed the largest mean value and the smallest variability of total connectivity (fig. S3H).

Statistics

Values are given as mean ± standard error of the mean (SEM). Box plots show the lower quartile (Q1), the median (horizontal black line) and the upper quartile (Q3). Thus, the interquartile range (IQR = Q3–Q1) is represented as the height of the box. Whiskers extend to the most extreme data point that is no more than 1.5 x IQR from the edge of the box (Tukey style). Significance of differences was assessed by two-tailed Mann-Whitney test at the significance level (P) indicated (*57*). Membrane potentials reported in the text were not corrected for junction potentials.

To test whether reciprocal, convergence, divergence, and disynaptic chain motifs occurred significantly more frequently than expected by chance, we simulated the entire set of recording configurations (72 octuples, 66 septuples, 118 sextuples, 120 quintuples, 135 quadruples, 96 triples, and 495 double recordings) 10,000 times, assuming random connectivity (*58*). The connection probability was set to the experimentally determined average value of 0.92%. Statistical P values were calculated as the number of simulated configurations in which the motif number was equal to or larger than the empirical number, divided by the number of simulations (10,000).

MODELING

Basic structure of the CA3 network model

Simulations of pattern completion in autoassociative memory network models were performed following previous work (*9*, *11*, *14*, 59) (table S3). The hallmark properties of the network were: usage of binary neurons, recurrent excitatory connectivity, clipped Hebbian plasticity, global threshold, linear global inhibition (proportional to total network activity), and iterative recall (Fig. 5A). Computations were run in three steps: (1) definition of connectivity matrix *W*, (2) storage of random patterns via synaptic plasticity (resulting in a synaptic weight matrix *J*), and (3) simulation of iterative recall triggered by degraded patterns.

As finite-size effects are likely to be important (*60*), we modeled the network in realistic size. The total number of excitatory neurons n was 330,000, representing the CA3 pyramidal cell network of one hemisphere. In a subset of simulations, models of double size (with 2 x 330,000 = 660,000 neurons) were implemented, to represent the activity of left and right hippocampus with contralateral connectivity (fig. S11, A and B). Furthermore, models of one third of original size (110,000 neurons) were tested, to evaluate pattern completion in an isolated CA3b region (fig. S11, C and D).

To define the connectivity matrix *W* of size n x n, neurons were connected according to three different connectivity rules. First, neurons were connected randomly (*58*), assuming a uniform connection probability (p) and exclusion of autapses. Second, reciprocal, convergence, divergence, and disynaptic chain motifs were included. To achieve this, we used a SONET algorithm (*34*), setting α_{recip}, α_{conv}, α_{div}, and α_{chain} to values > 0, where α describes the enrichment of a given motif above the random level. Finally, in a subset of simulations, connectivity was restricted to two thirds of the network by eliminating connections from the matrix *W*, to account for the limited extent of CA3 pyramidal neuron axons along the septo-temporal axis (*35*, *36*) (fig. S10).

Storage in the network model

To simulate storage of information, random activity patterns were applied to the network. Patterns were vectors of binary numbers of length n, in which 0 represented inactivity and 1 action potential firing. The total average activity level f was assumed as 0.001 (see Refs *13*, *14*, *58*), consistent with sparse firing of CA3 pyramidal neurons *in vivo* in non-sharp wave ripple periods during < 10-ms time intervals (*61*). Thus, for a 330,000 neuron network, a pattern vector contained on average 330 values of 1 and 329,670 values of 0. Before storage, the network was initialized by setting all elements of synaptic weight matrix *J* to 0.

An increasing number (m) of random binary patterns was then loaded into the network. Synaptic plasticity was implemented using a clipped Hebbian rule (*8, 60*). When both pre- and postsynaptic neurons were simultaneously active during a pattern, synaptic weights were updated to 1; otherwise weights were unchanged. The use of this rule was justified by experimental data, demonstrating both requirement for simultaneous pre- and postsynaptic activity and saturation of the extent of LTP at recurrent CA3–CA3 synapses (*33*). Mathematically, the synaptic weight matrix *J* was computed as the sum of the outer products of the pattern vectors, clipped at a maximal value of 1.

Recall in the network model

To simulate iterative recall, a subset (100) of the activity patterns originally applied in the storage phase was re-applied to the network. Patterns applied during recall were degraded in comparison to the original ones applied during storage. The proportion of validly firing neurons (b_{valid}) was 0.5 and the proportion of spuriously firing neurons ($b_{spurious}$) was 0.001, corresponding to a correlation between original and degraded patterns of 0.71. We then simulated the ability of the network to iteratively recall the original patterns (*14*, 62). Neuronal activity was computed over 10 or 50 recall cycles (*62*). For each recall cycle, the total input to the i^{th} neuron at time t was calculated as

$$h_i(t) = \frac{1}{n} \sum_{j=1}^{n} (W_{ij}\ J_{ij}\ P_{ij})\ X_j(t), \qquad \text{(Eq. 1)}$$

where *W* denotes the connectivity matrix, *J* represents synaptic weight matrix, P is a matrix incorporating synaptic variability, and *X*(t) is the network activity vector at time t (*59*). *W*, *J*, and *P* were multiplied in an element-wise manner. The matrix P was introduced to take into account the stochastic nature of transmitter release (i.e. synaptic amplitude fluctuations from trial to trial, including failures) (*14*). Random numbers had a mean value I_μ, a standard deviation I_σ, and a coefficient of variation CV = I_σ / I_μ. In the default parameter set, I_μ was set to 1, and CV was set to 0 or 1.

During iterative recall, a neuron was assumed to fire action potentials at time t + 1 if the condition

$$h_i(t) - \frac{1}{n}\ g_1 S\ (t) > g_0 \qquad \text{(Eq. 2)}$$

was met, where S(t) = $\sum_{j=1}^{n} S_j(t)$ is the total activity, g_1 is the proportionality factor of inhibition, and g_0 is firing threshold (*59*). g_1 was varied between 0 and 0.05. In the default parameter setting, g_0 was assumed as 7 10^{-6}, corresponding to three excitatory synaptic inputs. To explore the parameter space, parameters of the model were varied over a wide range in comparison to the default values (table S3, right column).

Analysis of pattern correlation and capacity

To quantify the accuracy of recall of a given pattern, pattern correlation (*r*) between original and recalled patterns was computed as the correlation coefficient between the corresponding vectors (*57*, *59*). Pattern correlation was quantified for the 8th recall cycle, since steady-state conditions were nearly reached for this cycle (*62*; Fig. 5A). Pattern correlation r was then plotted against the pattern load m and the

proportionality factor of inhibition g_1. These 3-dimensional r–m–g_1 plots (e.g. Fig. 5) provided information about capacity, robustness of recall, and maximal correlation.

Capacity (in number of patterns) was quantified as the maximum of the product function of pattern correlation (r) and pattern load (m). This definition was chosen to take into account both the number of patterns that can be stored and accurately recalled and the recall accuracy of these patterns. Robustness of pattern completion was quantified as the area enclosed by the 50% contour line in the r–m–g_1 plots. Information capacity (in bit synapse^{-1}) was calculated as

$$i = \frac{N_{patterns}\,(-f\log_2 f - (1-f)\log_2(1-f))}{n\,p}, \qquad \text{(Eq. 3)}$$

where $N_{patterns}$ is capacity, f is activity level, n is the number of neurons, and p is connection probability (e.g. *60*).

Simulations of random connectivity matrices, storage, and iterative recall were implemented in C or C++, and run on x86_64-based shared memory systems (Supermicro or SGI Altix UV 1000 systems) using GNU/Linux (Debian, SLES), the GNU C compiler (GCC, 4.3.4, 4.9.2), and the GNU scientific library (GSL, 1.11, 1.16). Simulations were run with up to 20 different seeds. Connectivity matrices containing disynaptic connectivity motifs were generated using the SONET simulation program package (*34*) after minor modifications. Changes included improvement in memory management, storage of matrices in sparse format, and adaptation to a 64-bit computation platform. Computer source code will be provided upon request.

References and Notes

1. H. Eichenbaum, *Neuron* **44**, 109–120 (2004).
2. R. P. Kesner, *Learn. Mem.* **14**, 771–781 (2007).
3. B. L. McNaughton, R. G. M. Morris, *Trends Neurosci.* **10**, 408–415 (1987).
4. A. Treves, E. T. Rolls, *Hippocampus* **4**, 374–391 (1994).
5. J. E. Lisman, *Neuron* **22**, 233–242 (1999).

6. K. Nakazawa, T. J. McHugh, M. A. Wilson, S. Tonegawa, *Nat. Rev. Neurosci.* **5**, 361–372 (2004).
7. J. P. Neunuebel, J. J. Knierim, *Neuron* **81**, 416–427 (2014).
8. D. J. Willshaw, O. P. Buneman, H. C. Longuet-Higgins, *Nature* **222**, 960–962 (1969).
9. D. Marr, *Philos. Trans. R. Soc. Lond. B Biol. Sci.* **262**, 23–81 (1971).
10. G. Palm, *Biol. Cybern.* **36**, 19–31 (1980).
11. J. J. Hopfield, *Proc. Natl. Acad. Sci. USA* **79**, 2554–2558 (1982).
12. H. Sompolinsky, *Phys. Rev. A Gen. Phys.* **34**, 2571–2574 (1986).
13. D. J. Amit, H. Gutfreund, H. Sompolinsky, *Phys. Rev A* **35**, 2293–2303 (1987).
14. M. R. Bennett, W. G. Gibson, J. Robinson, *Philos. Trans. R. Soc. Lond. B Biol. Sci.* **343**, 167–187 (1994).
15. R. Miles, R. K. S. Wong, *J. Physiol.* **373**, 397–418 (1986).
16. R. D. Traub, R. Miles, *Neuronal Networks of the Hippocampus.* Cambridge University Press, Cambridge (1991).
17. R. Perin, T. K. Berger, H. Markram, *Proc. Natl. Acad. Sci. USA* **108**, 5419–5424 (2011).
18. S. Song, P. J. Sjöström, M. Reigl, S. Nelson, D. B. Chklovskii, *PLoS Biol.* **3**, e68 (2005).
19. S. Rieubland, A. Roth, M. Häusser, *Neuron* **81**, 913–929 (2014).
20. D. J. Watts, S. H. Strogatz, *Nature* **393**, 440–442 (1998).
21. J. Lübke, H. Markram, M. Frotscher, B. Sakmann, *J. Neurosci.* **16**, 3209–3218 (1996).
22. H. Markram, J. Lübke, M. Frotscher, A. Roth, B. Sakmann, *J. Physiol.* **500**, 409–440 (1997).
23. T. Branco, K. Staras, *Nat. Rev. Neurosci.* **10**, 373–383 (2009).
24. A. I. Gulyás *et al.*, *Nature* **366**, 683–687 (1993).
25. N. Holderith *et al.*, *Nat. Neurosci.* **15**, 988–997 (2012).
26. R. A. Silver, J. Lübke, B. Sakmann, D. Feldmeyer, *Science* **302**, 1981–1984 (2003).

27. N. Spruston, P. Jonas, B. Sakmann, *J. Physiol.* **482**, 325–352 (1995).
28. Z. Nusser *et al.*, *Neuron* **21**, 545–559 (1998).
29. J. Kowalski, J. Gan, P. Jonas, A. J. Pernía-Andrade, *Hippocampus* **26**, 668–682 (2016).
30. S. Cash, R. Yuste, *Neuron* **22**, 383–394 (1999).
31. S. Kim, S. J. Guzman, H. Hu, P. Jonas, *Nat. Neurosci.* **15**, 600–606 (2012).
32. D. G. Amaral, N. Ishizuka, B. Claiborne, *Prog. in Brain Res.* **83**,1–11 (1990).
33. R. K. Mishra, S. Kim, S. J. Guzman, P. Jonas, *Nat. Commun.* ***7****, 11552* (2016).
34. L. Zhao, B. Beverlin II, T. Netoff, D. Q. Nykamp, *Front. Comput. Neurosci.* **5**, 28 (2011).
35. X. G. Li, P. Somogyi, A. Ylinen, G. Buzsáki, *J. Comp. Neurol.* **339**, 181–208 (1994).
36. M. P. Witter, *Learn Mem.* **14**, 705-713 (2007).
37. E. T. Rolls, *Front. Syst. Neurosci.* **7**, 74 (2013).
38. S. Lefort, C. Tomm, J. C. Floyd Sarria, C. C. Petersen, *Neuron* **61**, 301–316 (2009).
39. N. Brunel, *Nat. Neurosci.* **19**, 749–755 (2016).
40. Y. Deguchi, F. Donato, I. Galimberti, E. Cabuy, P. Caroni, *Nat. Neurosci.* **14**, 495–504 (2011).
41. Y. C. Yu, R. S. Bultje, X. Wang, S. H. Shi, *Nature* **458**, 501–504 (2009).
42. F. Engert, T. Bonhoeffer, *Nature* **399**, 66–70 (1999).
43. D. A. Henze, L. Wittner, G. Buzsáki, *Nat. Neurosci.* **5**, 790–795 (2002).
44. N. P. Vyleta, P. Jonas, *Science* **343**, 665–670 (2014).
45. A. Mitra, S. S. Mitra, R. W. Tsien, *Nat. Neurosci.* **15**, 250–257 (2011).
46. J. E. Hanson, M. Blank, R. A. Valenzuela, C. C. Garner, D. V. Madison, *J. Physiol.* **579**, 53–67 (2007).
47. J. J. Couey *et al.*, *Nat. Neurosci.* **16**, 318–324 (2013).

Supplementary References

48. J. Bischofberger, D. Engel, L. Li, J. R. P. Geiger, P. Jonas, Patch-clamp recording from mossy fiber terminals in hippocampal slices. *Nat. Protoc.* **1**, 2075–2081 (2006).

49. S. J. Guzman, A. Schlögl, C. Schmidt-Hieber, Stimfit: quantifying electrophysiological data with Python. *Front. Neuroinform.* **8**, 16 (2014).

50. U. Kraushaar, P. Jonas, Efficacy and stability of quantal GABA release at a hippocampal interneuron-principal neuron synapse. *J. Neurosci.* **20**, 5594–5607 (2000).

51. L. Wittner, D. A. Henze, L. Záborszky, G. Buzsáki, Three-dimensional reconstruction of the axon arbor of a CA3 pyramidal cell recorded and filled in vivo. *Brain Struct. Funct.* **212**, 75 –83 (2007).

52. N. T. Carnevale, M. L. Hines, *The Neuron Book.* Cambridge University Press, Cambridge, UK (2006).

53. P. Jonas, G. Major, B. Sakmann, Quantal components of unitary EPSCs at the mossy fibre synapse on CA3 pyramidal cells of rat hippocampus. *J. Physiol.* **472**, 615–663 (1993).

54. G. Major, A. U. Larkman, P. Jonas, B. Sakmann, J. J. B. Jack, Detailed passive cable models of whole-cell recorded CA3 pyramidal neurons in rat hippocampal slices. *J. Neurosci.* **14**, 4613–4638 (1994).

55. C. Schmidt-Hieber, P. Jonas, J. Bischofberger, Subthreshold dendritic signal processing and coincidence detection in dentate gyrus granule cells. *J. Neurosci.* **27**, 8430–8441 (2007).

56. D. Ropireddy, R. Scorcioni, B. Lasher, G. Buzsáki, G. A. Ascoli, Axonal morphometry of hippocampal pyramidal neurons semi-automatically reconstructed after in vivo labeling in different CA3 locations. *Brain. Struct. Funct.* **216**, 1–15 (2011).

57. J. H. Zar, *Biostatistical analysis*. Prentice Hall, 5th edition, New Jersey (2010).

58. P. Erdös, A. Rényi, On random graphs. I. *Publicationes Mathematicae* **6**, 290–297 (1959).

59. W. G. Gibson, J. Robinson, Statistical analysis of the dynamics of sparse associative memory. *Neural Networks* **5**, 645–661 (1992).
60. A. M. Dubreuil, Y. Amit, N. Brunel, Memory capacity of networks with stochastic binary synapses. PLoS Comput. Biol. **10**, e1003727 (2014).
61. J. Csicsvari, H. Hirase, A. Mamiya, G. Buzsáki, Ensemble patterns of hippocampal CA3-CA1 neurons during sharp wave-associated population events. *Neuron* **28**, 585–594 (2000).
62. F. Schwenker, F. T. Sommer, G. Palm, Iterative retrieval of sparsely coded associative memory patterns. *Neural Networks* **9**, 445–455 (1996).
63. B. A. MacVicar, F. E. Dudek, Dye-coupling between CA3 pyramidal cells in slices of rat hippocampus. *Brain Res.* **196**, 494–497 (1980).
64. M. Tsodyks, M. Feigel'man, Enhanced storage capacity in neural networks with low level of activity. *Europhysics Letters* **6**, 101–105 (1988).
65. A. Treves, E. T. Rolls, What determines the capacity of autoassociative memories in the brain? *Network* **2**, 371–397 (1991).
66. G. Palm, Memory capacities of local rules for synaptic modification. *Concepts in Neuroscience* **2**, 97–128 (1991).
67. N. Brunel, Storage capacity of neuronal networks: effect of the fluctuations of the number of active neurons per memory. *J. Phys. A: Math Gen.* **27**, 4783–4789 (1994).
68. E. Gardner, *J. Phys. A Math. Gen.* **21**, 257–270 (1988).

Fig. S1. Selective labeling of synaptically connected cells in octuples.

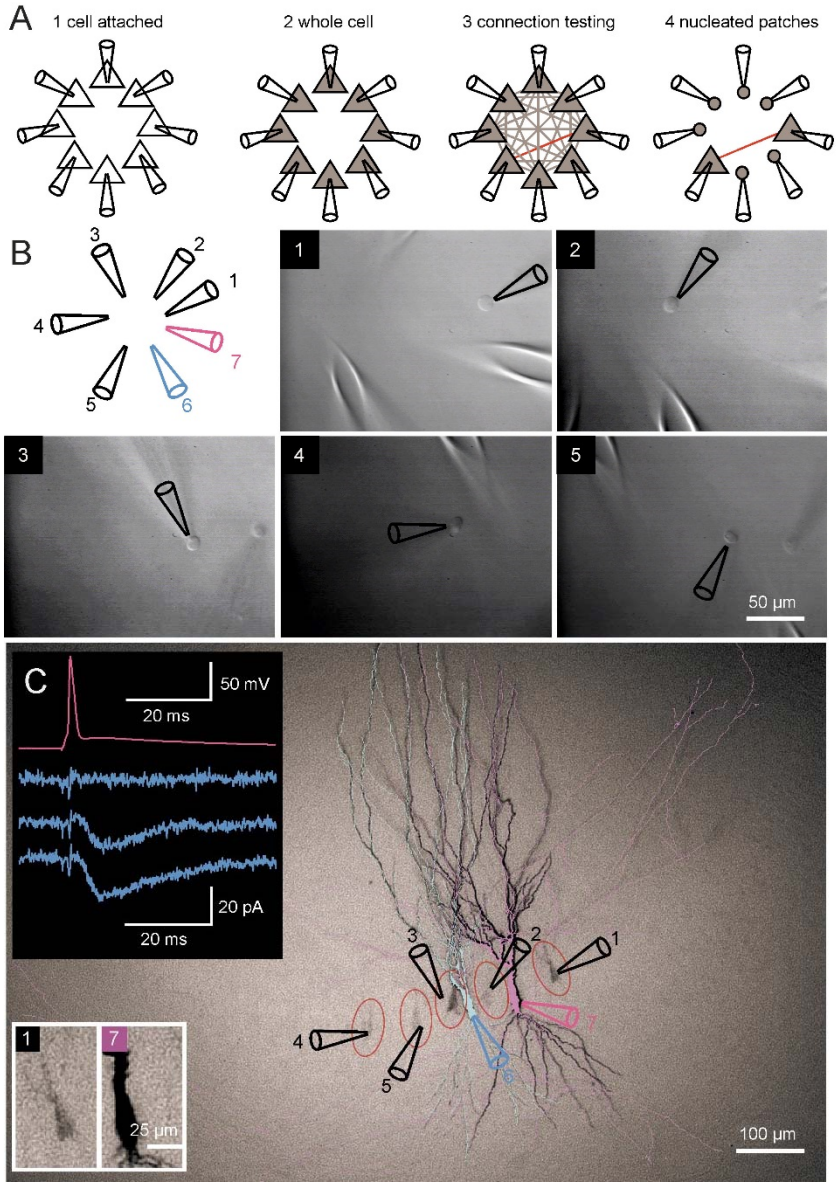

(**A**) A four-step procedure to achieve selective labeling of connected neurons. (1) Tight seal cell-attached configurations were obtained in all eight neurons. (2) The transition into the whole-cell configuration was made nearly simultaneously in all cells. (3) All pairs of cells were tested for possible connections. (4) Nucleated patches were isolated from the non-connected cells to avoid further loading with biocytin. The whole-cell configuration was maintained only in the synaptically connected cells, resulting in selective labeling of pre- and postsynaptic neuron.
(**B**) Destaining by nucleated patch formation. Identification of synaptically connected cells (cells 6 and 7) and formation of nucleated patches in unconnected

cells (cells 1–5) in a septuple recording configuration. Note that pipette location and angle allowed unequivocal assignment of the cells.
(**C**) Biocytin labeling after destaining procedure shown in (B). Intense labeling allowed full digital reconstruction of postsynaptic cell (cell 6, cyan) and presynaptic cell including axon (cell 7, magenta). In contrast, perisomatic labeling was faint or absent in the non-connected cells (red ellipses). Large inset shows single traces from a synaptic connection between cell 7 (magenta) and cell 6 (cyan), showing a functional connection. Small inset illustrates perisomatic areas of cell 1 (unconnected, faint labeling) and cell 7 (connected, intense labeling).

Fig. S2. Chemical versus electrical coupling between CA3 pyramidal neurons.

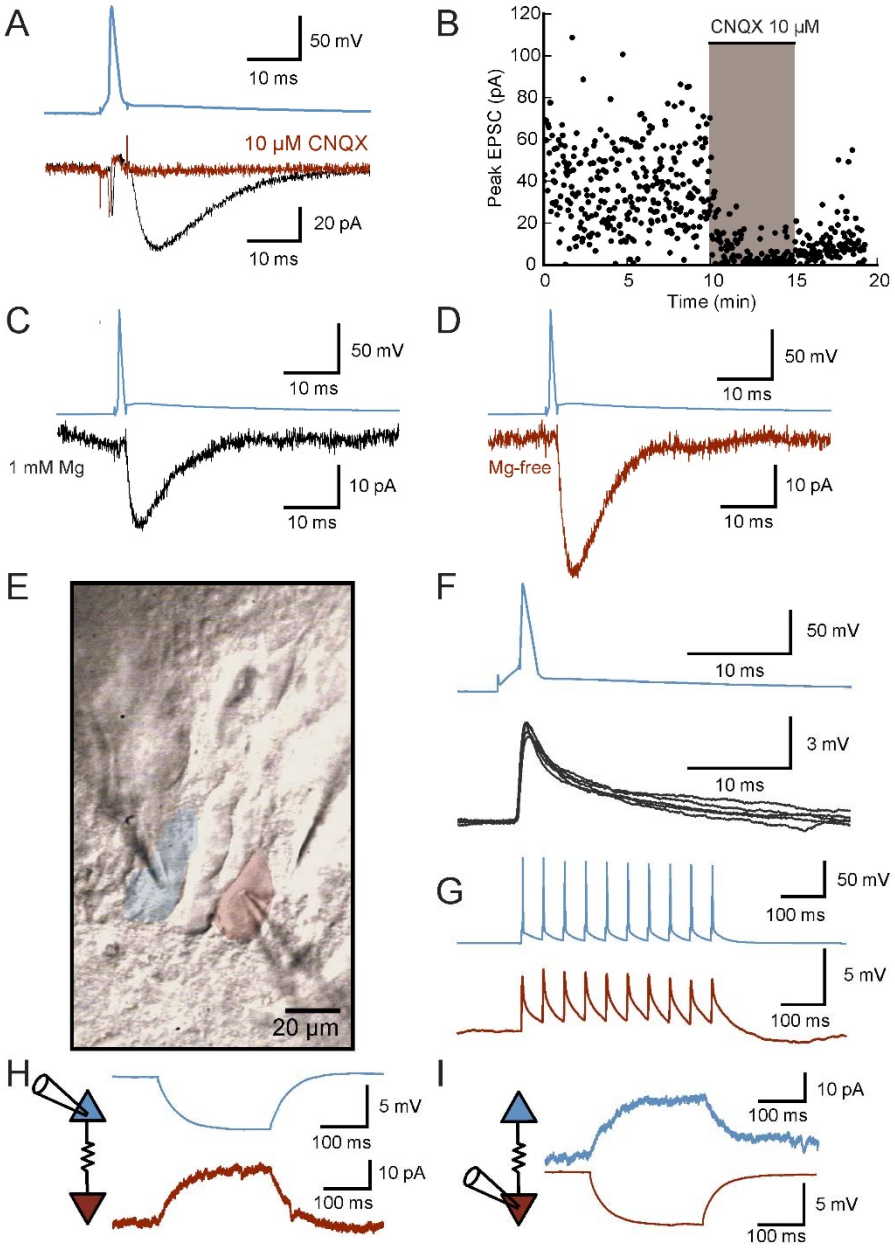

(**A** to **D**) Chemical synaptic transmission.
(**A**) Unitary EPSCs at CA3–CA3 synapses under control conditions (black trace) and in the presence of 10 μM CNQX (red trace; postsynaptic membrane potential –70 mV).
(**B**) Corresponding plot of unitary EPSC peak amplitude against experimental time during application of 10 μM CNQX (gray area). Note that CNQX completely

blocked unitary EPSCs, indicating that transmission was chemical in nature and mediated by AMPA-type glutamate receptors.
(**C** and **D**) Unitary EPSCs in control conditions (C) and in Mg^{2+}-free extracellular solution (D). EPSC amplitude increases in the absence of Mg^{2+}, suggesting a contribution of NMDA-type glutamate receptors to the synaptic current.
Chemical transmission was found in 146 out of 15,930 tested pairs.
(**E** to **I**) Electrical synaptic transmission.
(**E**) Infrared differential interference contrast image of two CA3 neurons electrically connected, presumably via a gap junction. Blue and red areas represent the 2D projections of the two cell bodies.
(**F** and **G**) Postsynaptic voltage changes in response to a single action potential (F; 5 consecutive traces) and a train of 10 action potentials (G). Note that the postsynaptic response shows almost constant amplitude in consecutive trials, as characteristic for electrical synaptic transmission.
(**H** and **I**) Current changes in a CA3 pyramidal neuron evoked in response to a long hyperpolarizing current pulse (50 pA, 250 ms) applied to the other cell. Current injection was made either in the blue cell (H) or the red cell (I). All traces were taken from the same CA3–CA3 pair (in a slice from a 16-day-old rat).
Evidence for electrical coupling was found in one out of 15,930 tested pairs (*63*).

Fig. S3. Connectivity in transverse, parasagittal, and frontal slices.

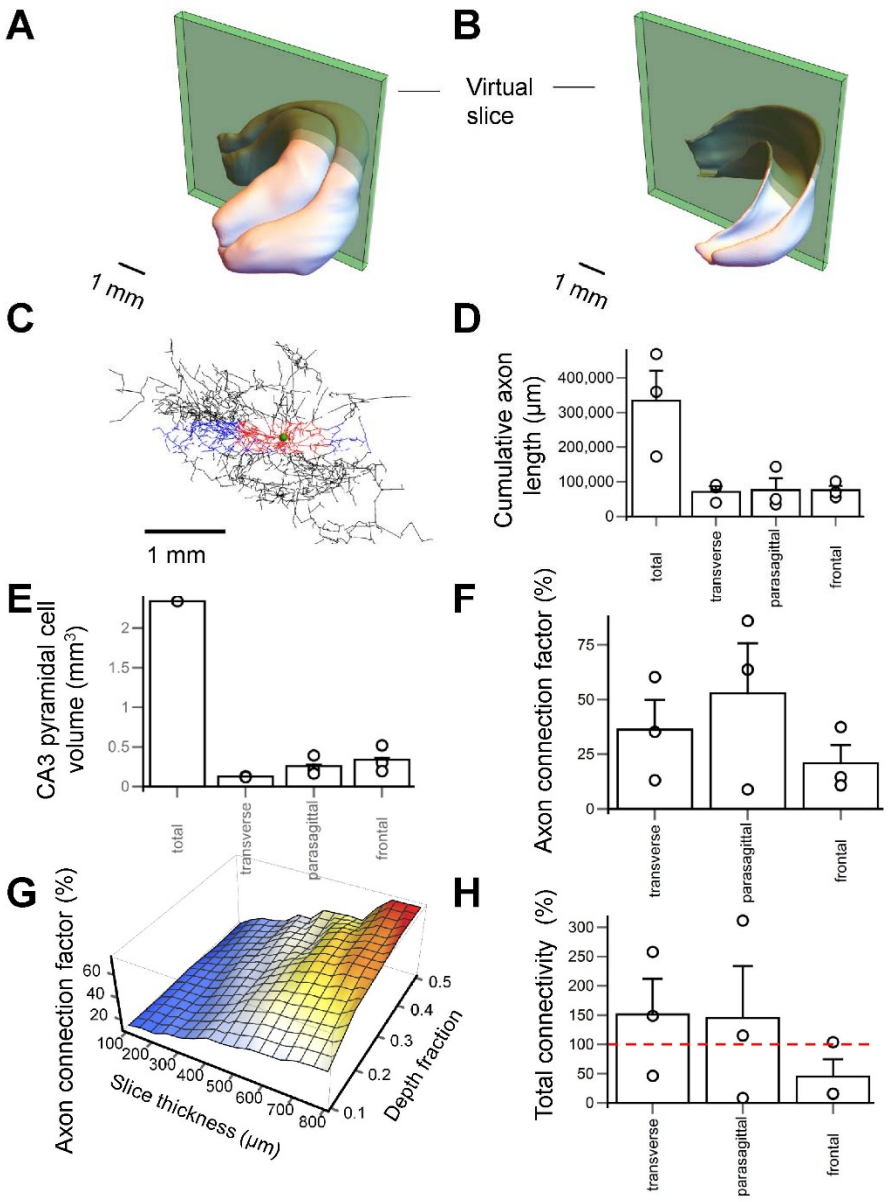

(**A** and **B**) "Virtual slicing" procedure. Surface graphics of the dentate gyrus and the CA3 and CA1 regions of the hippocampus (somatic and dendritic layers; (A)) and the CA3 and CA1 pyramidal neuron layer (B), superimposed with a 400-µm slice close to the transverse plane (α = 0; β = –5°) (*48*, *56*).
(**C**) Axonal arborization of a fully reconstructed CA3b pyramidal neuron (cell 51) (*56*). View from anterior direction. Blue and red, axon segments contained in a simulated 400-µm thick transverse slice (red, within a 600-µm radius from the soma; blue, outside a 600-µm radius). Black, axon segments outside the simulated slice. Green sphere represents cell body.

(**D** and **E**) Summary bar graph of cumulative axon length (D), and corresponding volume of the CA3 pyramidal neuron layer (E). Total, value for the intact brain; transverse, parasagittal, and frontal, values for simulated 400-µm sections of different orientations. Data were obtained from three different CA3 pyramidal neurons (cell 51, D256, and 60a) (*56*). Note that slicing decreased both the cumulative axon length and the CA3 pyramidal cell layer volume, so that the ratio was relatively unaltered by the slicing procedure.
(**F** and **G**) Axon connection factor, i.e. fraction of axon segments connected to the soma over total number of axon segments, for 400-µm slices with soma in the center (F) and for different slice thicknesses and depth fractions (0 = surface, 0.5 = center of the slice; average data from three cells and orientations; G). Note that axons crossing the surface of the virtual slice section were disconnected from the soma, so that the axon connection factor was significantly below 100%. Only axon segments within a 600-µm radius from the soma were considered.
(**H**) Total connectivity, obtained as fraction of preserved axon / fraction of preserved pyramidal cell volume x axon connection factor for 400-µm slices with soma in the center. Red dashed line indicates 100% predicted connectivity. Note that transverse slices showed high connectivity and relatively small variability (at least for the three analyzed cells; left bar), whereas connectivity was more variable in parasagittal slices (middle bar) and smaller in frontal slices (right bar).

Fig. S4. Detailed properties of macroconnectivity in the CA3 pyramidal cell network.

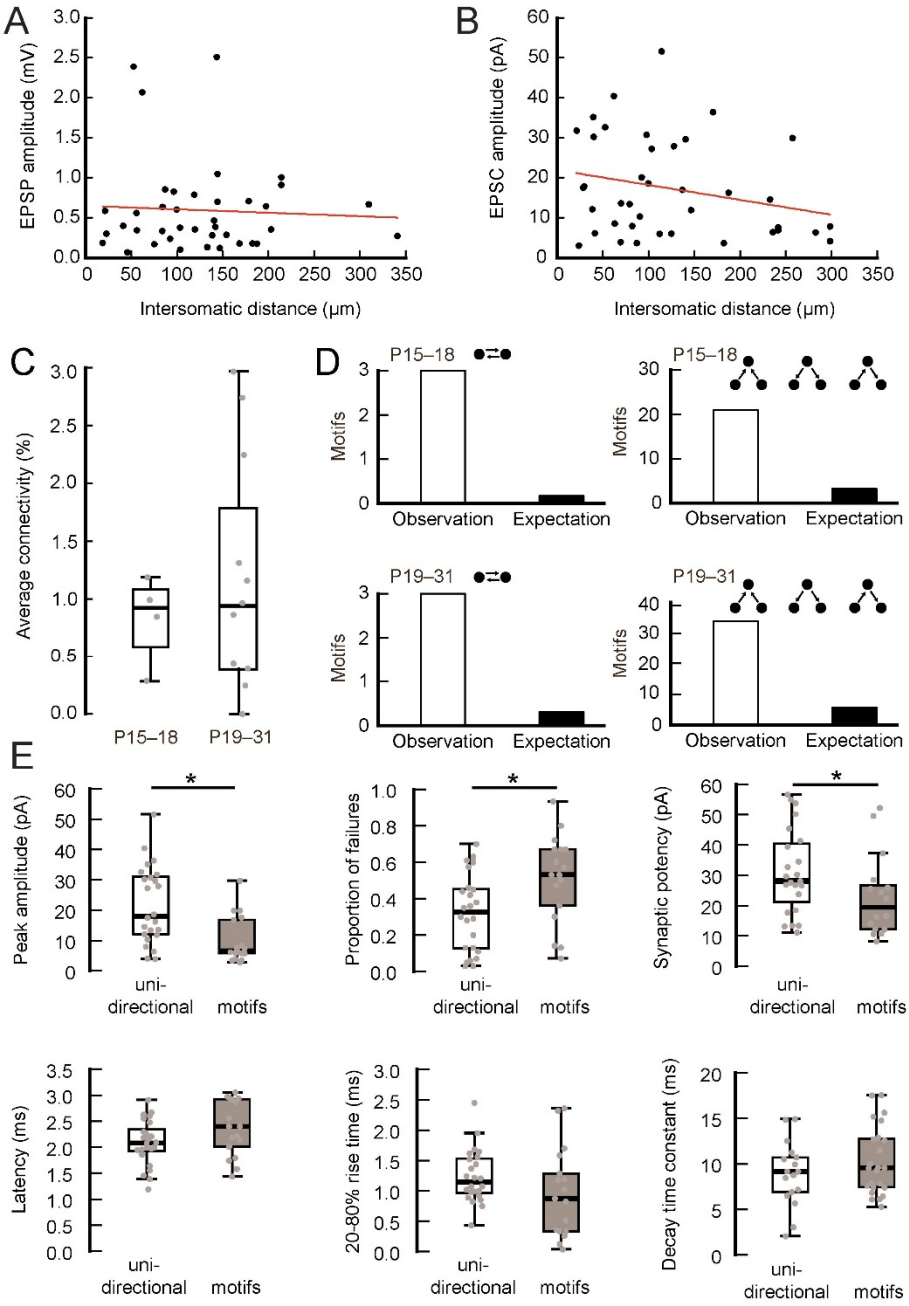

(**A** and **B**) Distance dependence of unitary EPSP (A) and EPSC peak amplitude (B). Red lines represent the result from linear regression; P = 0.74 and 0.13, respectively.
(**C**) Average connectivity for slices from young (P15–18) and older (P19–31) rats (P = 0.372). Open circles represent data for each 1-day age interval.

(**D**) Number of connectivity motifs in both age groups. Bar graphs show the number of a given motif in the experimental sample (open bars) and the predicted number in a network with random connectivity (filled bars).
(**E**) Properties of EPSCs from synaptic connections found in isolation (white boxes) and from synaptic connections embedded in disynaptic motifs (i.e. reciprocal, convergence, divergence, and chain motifs; gray boxes). Graphs show EPSC peak amplitude ($P < 0.001$), proportion of failures ($P = 0.002$), EPSC potency (i.e. amplitude of successes; $P = 0.016$), synaptic latency ($P = 0.063$), EPSC 20–80% rise time ($P = 0.060$), and EPSC decay time constant (monoexponential fitting; $P = 0.251$). Note that some of the unidirectional connections may belong to connectivity motifs that were not recorded during the experiment.
In box plots, horizontal lines represent median, boxes quartiles, whiskers most extreme data points ≤ 1.5 interquartile range from box edges, and single points data from individual experiments. Asterisks indicate $P < 0.05$.

Fig. S5. Minimal depletion and rapid pool refilling during repetitive stimulation.

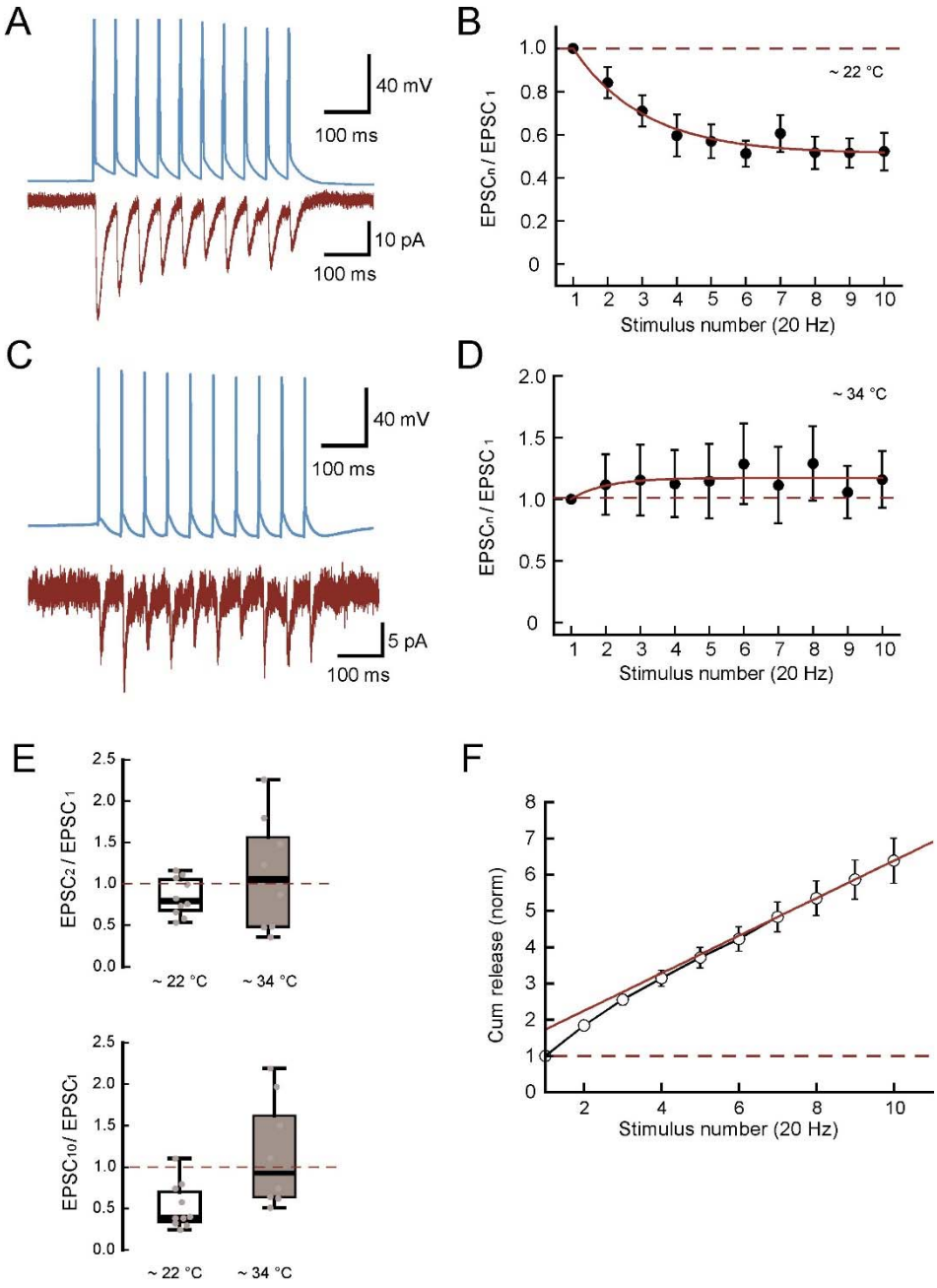

(**A**) Unitary EPSCs during train stimulation at 20 Hz at ~22°C. Top trace, presynaptic action potentials; bottom trace, average EPSC.
(**B**) Plot of $EPSC_n$ / $EPSC_1$, plotted against the number n of the stimulus. Red curve represents the results of curve fitting with a single exponential function with an offset. Mean values from 10 pairs at ~22°C.

(**C** and **D**) Similar data as shown in (A and B), but at near-physiological temperature (~34°C). Mean values from 9 pairs. Dashed lines in (B and D) indicate an $EPSC_n$ / $EPSC_1$ ratio of 1.
(**E**) Summary bar graph of results at ~22°C and ~34°C. Note moderate depression at ~22°C versus slight facilitation at ~34°C.
(**F**) Cumulative plot of EPSC peak amplitude against stimulus number (at ~22°C). Amplitude was normalized to that of the first stimulus. The last 5 data points were analyzed by linear regression. The offset was 1.71, and the slope was 1.21 $stimulus^{-1}$. For a number of functional release of 3.2 and a release probability of 0.37, this corresponds to a refilling rate of 1.43 $vesicles\ stimulus^{-1}$.

Fig. S6. Storage and recall of patterns in a real-size CA3 network model.

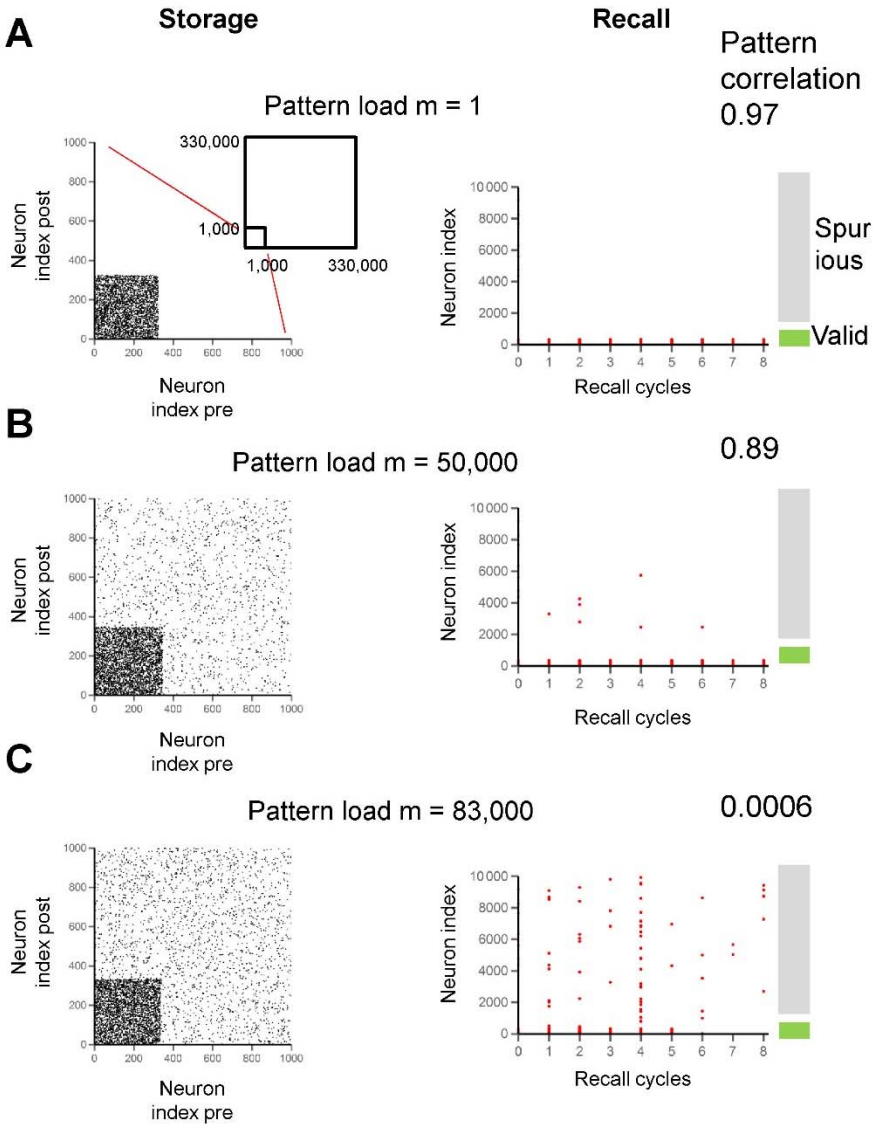

Storage was performed with a single test pattern with activity in the first 330 neurons and a variable number of subsequent random patterns. Recall was examined with the first pattern. Average activity level (f) was 0.001, similar to activity level in the first pattern (330 / 330,000). (**A**) Storage and recall of a single pattern in the network model. Left, elementwise product of connectivity matrix and synaptic weight matrix (*W J*) after storage of the first pattern; each black point represents a potentiated synapse in the matrix. Right, raster plot of neuron firing in the recall phase. Each red circle represents activity of a single neuron in the network. Recall was triggered with a degraded test pattern (b_{valid} = 0.5, $b_{spurious}$ = 0.001; correlation between original pattern and test pattern 0.71; see materials and

methods). Note the almost perfect recall of the original pattern (pattern correlation between retrieved pattern and test pattern at 8^{th} recall cycle 0.97, number on top). (**B**) Similar to (A), but after storage of 50,000 patterns in the network (pattern load m = 1 + 49,999). Note the accurate recall of the original pattern (pattern correlation between retrieved pattern and test pattern at 8^{th} recall cycle 0.89).
(**C**) Similar to (A), but after storage of 83,000 patterns in the network (pattern load m = 1 + 82,999). Note that the recall performance decreased, due to both lack of valid firings and generation of spurious firings (pattern correlation between retrieved pattern and test pattern at 8^{th} recall cycle 0.0006).
Total number of neurons in the network 330,000; only subsets of neurons (1,000 in left panels; 10,000 in right panels) are shown for clarity (see inset in (A), left). Connection probability p = 3%; random connectivity. Raster plots in (B) and (C) correspond to the plots of pattern correlation versus recall cycle shown in Fig. 5A.

Fig. S7. Dependence of pattern completion on total activity level.

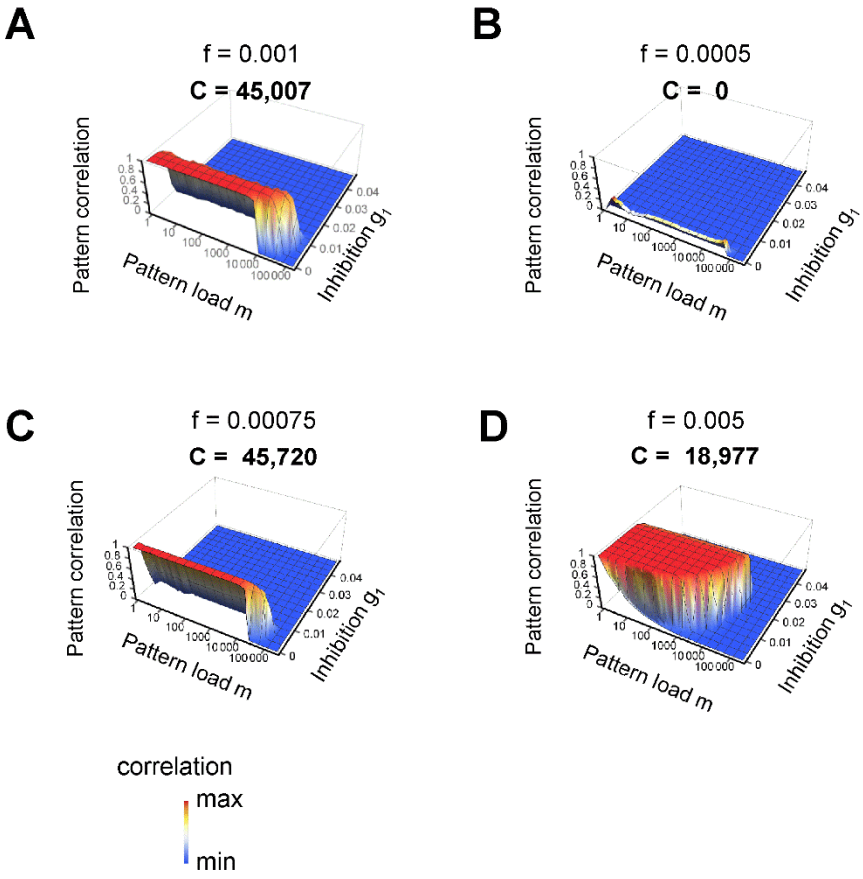

3D plots of pattern correlation versus pattern load (m) and inhibition factor (g_1) for connection probability p = 3% and different total activity levels f.
(**A**) f = 0.001 (standard parameter value).
(**B**) f = 0.0005.
(**C**) f = 0.00075.
(**D**) f = 0.005.
Random connectivity in all cases. Capacity (C) numbers indicate the maximum of m x r. Note that maximal capacity was obtained for an activity level f = 0.00075. For smaller activity levels, pattern completion failed because synaptic activity was below the activation threshold. For larger activity levels, capacity also decreased, consistent with previous theoretical studies (*13*, *64, 65*).

Fig. S8. Relative importance of reciprocity, convergence, divergence, and chain motifs for pattern completion.

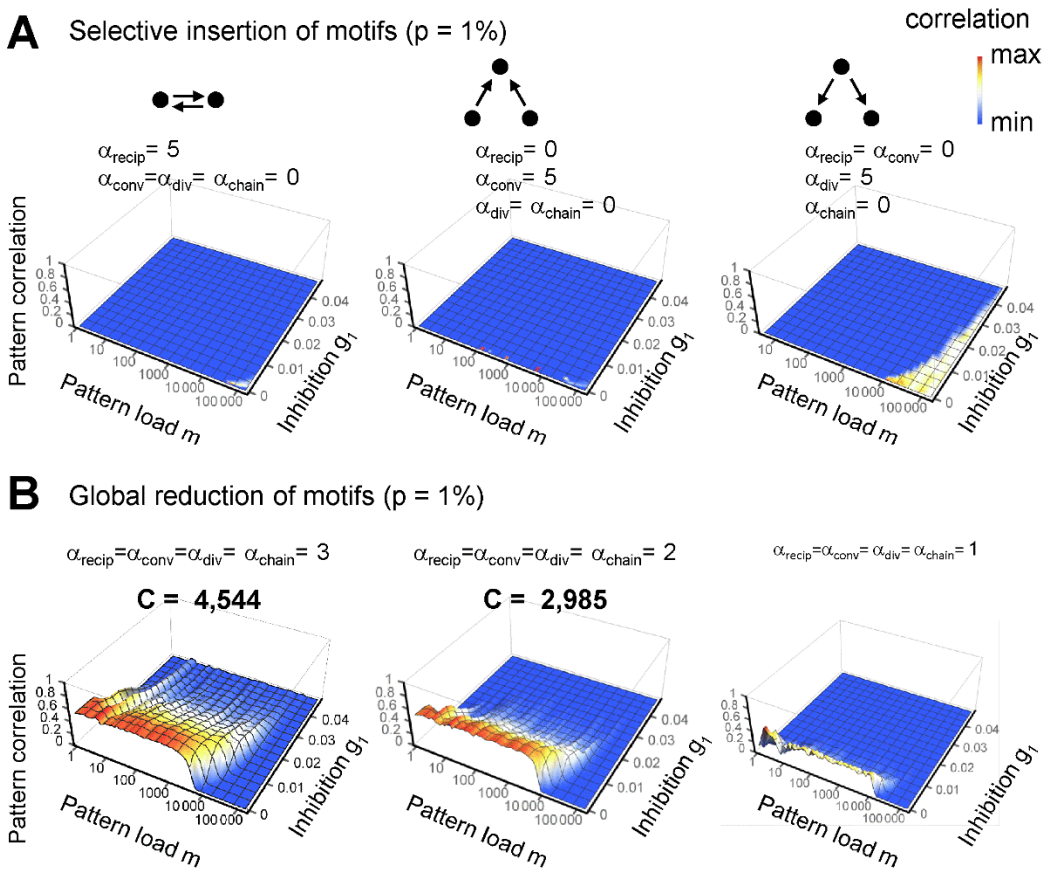

(**A**) Effects of selective incorporation of individual connectivity motifs. 3D plots of pattern correlation versus pattern load (m) and inhibition factor (g_1) for connection probability p = 1% and α_{recip} = 5, α_{conv} = 0, α_{div} = 0, and α_{chain} = 0 (left), α_{recip} = 0, α_{conv} = 5, α_{div} = 0, and α_{chain} = 0 (center), and α_{recip} = 0, α_{conv} = 0, α_{div} = 5, and α_{chain} = 0 (right). The network models were unable to generate pattern completion. For α_{recip} = α_{conv} = α_{div} = α_{chain} = 5, see Fig. 5C, center. Note that α_{recip} = α_{conv} = α_{div} = 0 and α_{chain} = 5 could not be tested, because this case does not give real solutions for the decomposition of the covariance matrix in the SONET algorithm (*34*).
(**B**) Effects of global reduction of connectivity motifs. 3D plot of pattern correlation versus pattern load (m) and inhibition factor (g_1) for connection probability p = 1% and α_{recip} = α_{conv} = α_{div} = α_{chain} = 3 (left), α_{recip} = α_{conv} = α_{div} = α_{chain} = 2 (center), and α_{recip} = α_{conv} = α_{div} = α_{chain} = 1 (right). Note that the performance of the pattern completion network gradually declined.

Fig. S9. Effects of motifs for different connection probability values.

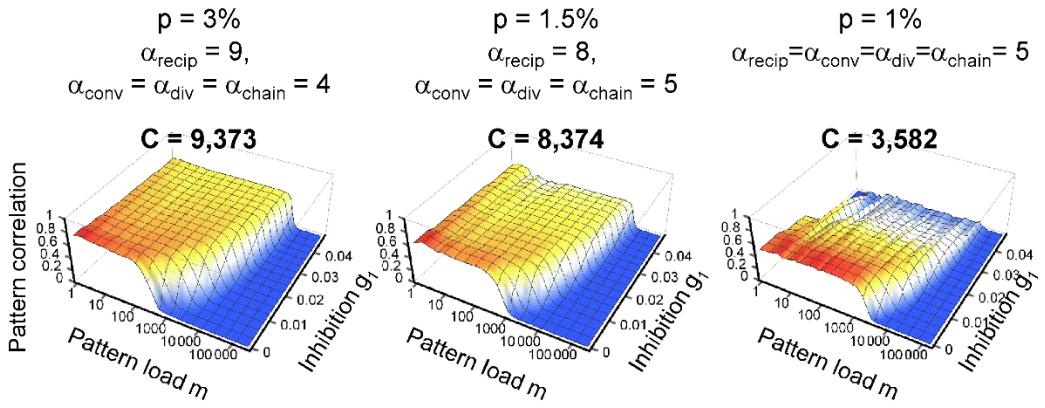

Effects of connectivity motifs for different connectivity p = 3% and α_{recip} = 9; α_{conv} = α_{div} = α_{chain} = 4 (left), p = 1.5% and α_{recip} = 8; α_{conv} = α_{div} = α_{chain} = 5 (center), and p = 1% and α_{recip} = α_{conv} = α_{div} = α_{chain} = 5 (right). Note that the same α values could not be tested, because these cases do not give real solutions for the decomposition of the covariance matrix in the SONET algorithm (*34*). For comparison with networks without motifs, see Fig. 5B.

Fig. S10. Sparsely connected real-size network models with limited axon projection produce pattern completion.

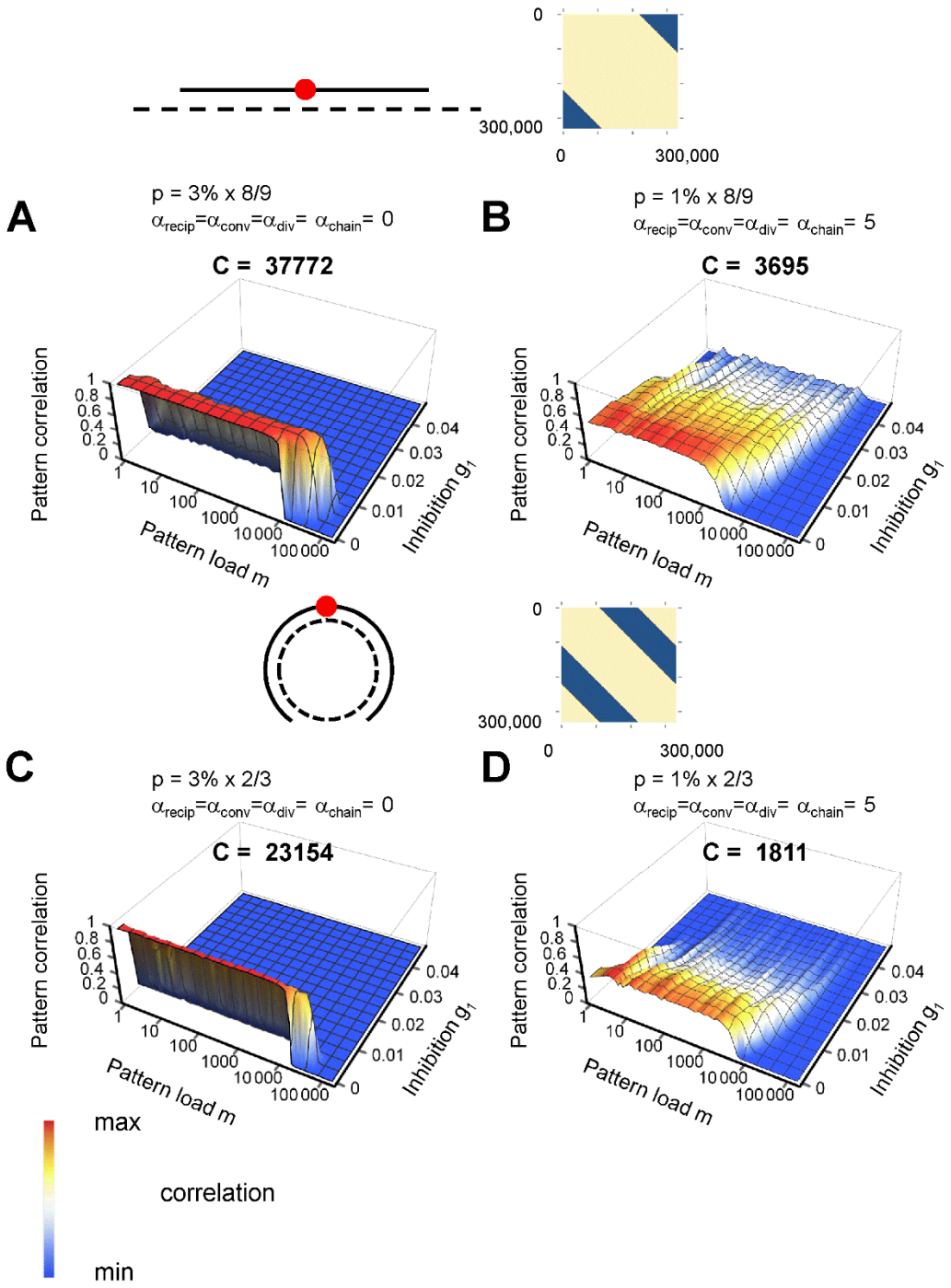

(**A** and **B**) 3D plots of pattern correlation versus pattern load (m) and inhibition factor (g_1) for networks in which axon arborization is confined to 2 / 3 of the

longitudinal axis. Connection probability p = 3% and random connectivity (A), connection probability 1% with $\alpha_{recip} = \alpha_{conv} = \alpha_{div} = \alpha_{chain} = 5$ (B).
(**C** and **D**) Similar analysis, but for circular arrangement of neurons and connectivity. For a connection probability of 1% and random connectivity, recall was not possible, neither in the linear nor in the circular case (capacity 0; not illustrated).
Schemes on top illustrate restricted connectivity (left) and corresponding connectivity matrices (right; yellow = possible connectivity; blue = no connectivity). Note that the basic properties of the network were similar to those of the network with unlimited axonal projection (Fig. 5, B and C).

Fig. S11. Sparsely connected network models of double and one-third size exhibit pattern completion.

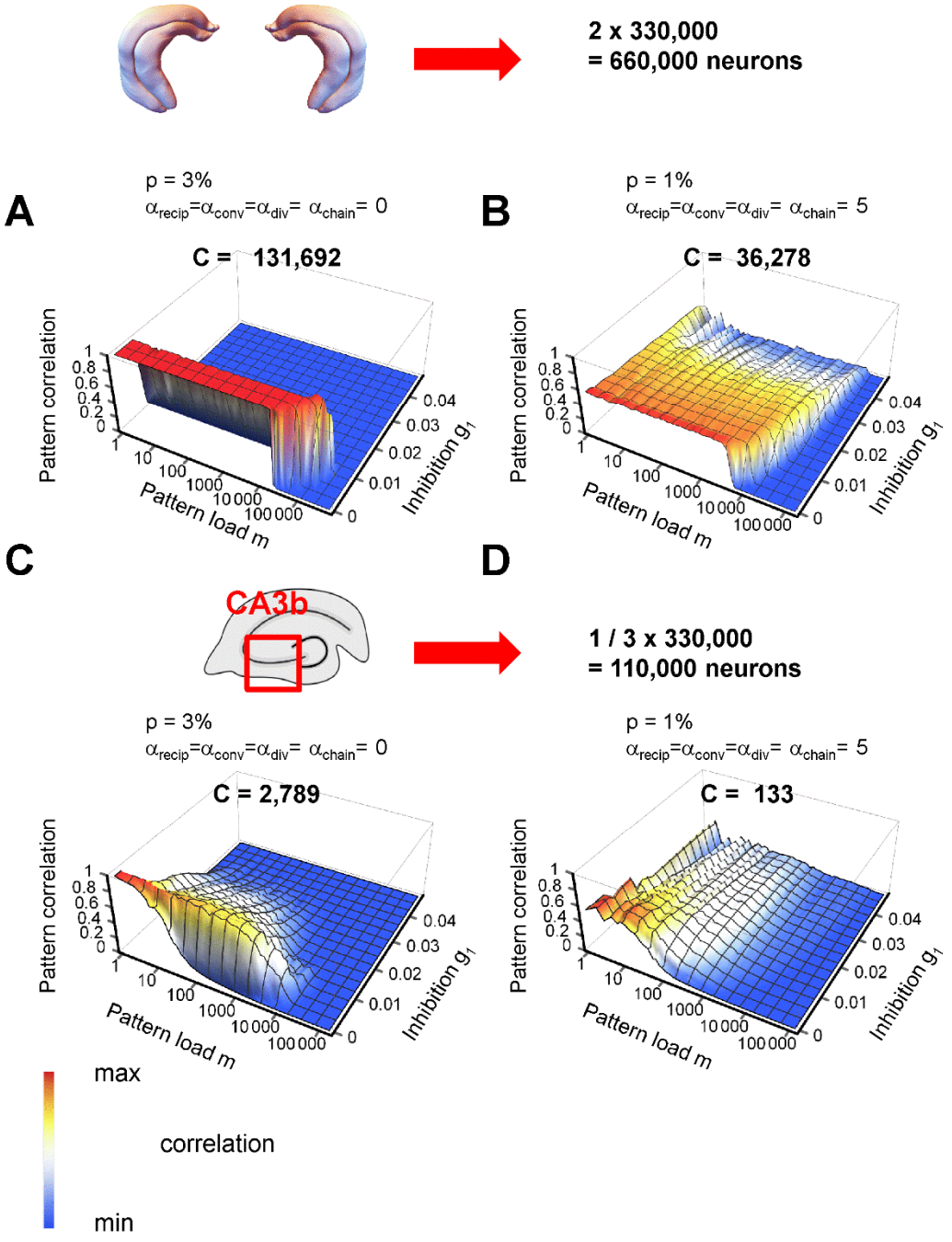

(**A** and **B**) Pattern completion in a double-size network model. 3D plots of pattern correlation versus pattern load (m) and inhibition factor (g_I) for connection probability p = 3% with random connectivity (A), and 1% with structured connectivity ($\alpha_{recip} = \alpha_{conv} = \alpha_{div} = \alpha_{chain} = 5$; B). In both simulations, the network

size was 2 x 330,000 = 660,000 neurons to represent two extensively interconnected hippocampal CA3 networks (scheme on top).
(**C** and **D**) Pattern completion in a one-third size network model. 3D plots of pattern correlation versus pattern load (m) and inhibition factor (g_1) for connection probability p = 3% with random connectivity (C), and 1% with structured connectivity ($\alpha_{recip} = \alpha_{conv} = \alpha_{div} = \alpha_{chain} = 5$; D). In both simulations, the network size was 1 / 3 x 330,000 = 110,000 neurons to depict the isolated CA3b subregion, from which the experimental data were obtained (scheme on top). Note that pattern completion was markedly impaired in the isolated CA3b subnetwork.

Table S1. Functional properties of unitary EPSPs and EPSCs at recurrent CA3–CA3 synapses.

Parameter	Value (~22°C)	Value (~34°C)
Resting membrane potential	68.2 ± 1.0 mV (n = 33)	
Action potential threshold	36.1 ± 1.6 mV (n = 33)	
EPSP peak amplitude	0.56 ± 0.01 mV (n = 40)	0.27 ± 0.1 mV (n = 5)
EPSP latency	2.3 ± 0.1 ms	1.2 ± 0.1 ms
EPSP 20–80% rise time	4.0 ± 0.2 ms	2.3 ± 0.4 ms
EPSP decay time constant	80.1 ± 6.2 ms	54.4 ± 6.8 ms
Failures	37 ± 3%	55 ± 11%
$EPSP_2$ / $EPSP_1$	0.84 ± 0.07 (n = 10)	1.15 ± 0.22 (n = 9)
$EPSP_{10}$ / $EPSP_1$	0.52 ± 0.07 (n = 10)	1.25 ± 0.23 (n = 9)
EPSC peak amplitude	17.3 ± 2.0 pA (n = 39)	14.4 ± 2.6 pA (n = 14)
EPSC latency	2.2 ± 0.1 ms	1.1 ± 0.1 ms
EPSC 20–80% rise time	1.1 ± 0.1 ms	1.1 ± 0.1 ms
EPSC decay time constant	9.5 ± 0.6 ms	8.7 ± 1.2 ms
Failures	40 ± 4%	43 ± 5%
$EPSC_2$ / $EPSC_1$	0.84 ± 0.07 (n = 10)	1.15 ± 0.22 (n = 9)
$EPSC_{10}$ / $EPSC_1$	0.52 ± 0.07 (n = 10)	1.25 ± 0.23 (n = 9)

Table S2. Multiple probability binomial analysis reveals a small number of functional release sites at recurrent CA3–CA3 synapses.

	q	**N**	**p_R 2 mM $[Ca^{2+}]_o$**	**p_R 1 mM $[Ca^{2+}]_o$**	**p_R 4 mM $[Ca^{2+}]_o$**	**CV_q**	**Number of connections**
EPSCs	4.41 ± 1.07 pA	2.75 ± 0.25	0.37 ± 0.04	0.18 ± 0.14	0.52 ± 0.07	0.79 ± 0.10	4
EPSPs	0.48 ± 0.09 mV	3.33 ± 0.41				0.69 ± 0.10	12

Table S3. Parameters of the network model of pattern completion.

Parameter	Explanation	Default value(s)	Alternative values or range (if indicated)
n	Number of neurons	330,000	165,000, 660,000
p	Connection probability	3, 1.5, or 1%	6%
f	Total activity level in pattern [1]	0.001	0.0005, 0.00075, 0.002, 0.005
g_0	Firing threshold	$7\ 10^{-6}$	$1\ 10^{-6}$, $10\ 10^{-6}$
g_1	Inhibition factor	0 – 0.05	
m	Pattern load (number of patterns applied in storage phase)	0 – 150,000	up to 580,000 in the largest networks
CV	Coefficient of variation of trial-to-trial fluctuations in synaptic events in recall phase	0 or 1	0.577, 0.707
b_{valid}	Proportion of valid firings in initial phase of recall (b_{valid} = 1 → identity to initial pattern)	0.5	0.75, 1
$b_{spurious}$	Proportion of spurious firings in initial phase of recall ($b_{spurious}$ = 0 → no spurious firing)	0.001	0.0005, 0
α_{recip}	Abundance of reciprocal motifs in comparison to random network (α = 0: random connectivity)	0 or 5	1, 2, 3
α_{conv}	Abundance of convergence motifs	0 or 5	1, 2, 3
α_{div}	Abundance of divergence motifs	0 or 5	1, 2, 3
α_{chain}	Abundance of disynaptic chains	0 or 5	1, 2, 3

1 Also referred to as fraction of active neurons or coding level (e.g. *39, 60*).

Table S4. Capacity of network models with different parameter settings.

Number of neurons (n)	Connectivity (p)	Activity (f)	Threshold (g_0)	CV	Initial pattern correlation r (b_{valid}, $b_{spurious}$)	Abundance of motifs (α)	Capacity (m x r) [1]	Information capacity (bits synapse^{-1})	α_c [2]	r_{max} [3]	Retrieval area [4]	Fig.
330,000	3%	0.001	7 10^{-6}	0	0.707 (0.5, 0.001)	All α = 0	45,007	0.0519	0.136	0.999	0.0519	5B left, S7A
165,000	3%	0.001	7 10^{-6}	0	0.707	All α = 0	8,964	0.0207	0.054	0.974	0.0207	
165,000	**6%**	0.001	7 10^{-6}	0	0.707	All α = 0	33,856	0.0390	0.205	1.0	0.0390	
660,000	3%	0.001	7 10^{-6}	0	0.707	All α = 0	131,098	0.0755	0.199	1.0	0.0755	
660,000	**1.5%**	0.001	7 10^{-6}	0	0.707	All α = 0	34,682	0.0400	0.053	0.971	0.0400	
330,000	3%	**0.0005**	7 10^{-6}	0	0.707	All α = 0	-	-	-	-	-	S7B
330,000	3%	**0.00075**	7 10^{-6}	0	0.707	All α = 0	45,720	0.0410	0.139	0.994	0.0254	S7C
330,000	3%	**0.005**	7 10^{-6}	0	0.707	All α = 0	18,977	0.0871	0.058	1.0	0.0871	S7D
330,000	3%	0.001	7 10^{-6}	0	**r = 0.816 (0.75,0.0005)**	All α = 0	65,498	0.0755	0.198	0.999	0.0755	
330,000	3%	0.001	7 10^{-6}	0	**r = 1 (1, 0), i.e. original pattern**	All α = 0	70,314	0.0810	0.213	0.998	0.0810	Foot notes 5, 6
330,000	3%	0.001	**1 10^{-6}**	0	0.707	All α = 0	14,004	0.0161	0.042	1.0	0.0161	
330,000	3%	0.001	**10 10^{-6}**	0	0.707	All α = 0	45,614	0.0526	0.138	0.995	0.0526	
330,000	**6%**	0.001	7 10^{-6}	0	0.707	All α = 0	33,856	0.0195	0.103	1.0	0.0195	
330,000	**1.5%**	0.001	7 10^{-6}	0	0.707	All α = 0	-	-	-	-	-	5B center
330,000	**1%**	0.001	7 10^{-6}	0	0.707	All α = 0	-	-	-	-	-	5B right
330,000	**1%**	0.001	7 10^{-6}	0	0.707	**All α = 5**	3,582	0.0124	0.012	0.536	0.1108	5C center S9C right
330,000	**1%**	0.001	7 10^{-6}	0	0.707	**All α = 3**	4,544	0.0157	0.005	0.564	0.0692	S8B left
330,000	**1%**	0.001	7 10^{-6}	0	0.707	**All α = 2**	2,985	0.0103	0.009	0.553	0.0384	S8B center
330,000	**1%**	0.001	7 10^{-6}	0	0.707	**All α = 1**	-	-	-	-	-	S8B right
330,000	**1.5%**	0.001	7 10^{-6}	0	0.707	**α_{recip} = 8; α_{conv} = α_{div} = α_{chain} = 5**	8,374	0.0193	0.025	0.685	0.0193	S9 center
330,000	**3%**	0.001	7 10^{-6}	0	0.707	**α_{recip} = 9; α_{conv} = α_{div} = α_{chain} = 4**	9,373	0.0108	0.028	0.764	0.0108	S9 left
330,000	3%	0.001	7 10^{-6}	**1.0**	0.707	All α = 0	7,037	0.0081	0.021	0.986	0.0081	5D center
330,000	3%	0.001	7 10^{-6}	**0.707**	0.707	All α = 0	15,095	0.0174	0.046	0.994	0.0174	
330,000	3%	0.001	7 10^{-6}	**0.577**	0.707	All α = 0	21,618	0.0249	0.066	0.997	0.0249	5D left

Left seven columns indicate parameters of the model. Right six columns indicate measured quantities and reference to Figures as applicable. First row indicates standard parameter values (red). Other rows indicate alterations of parameters (black on green background).

1 Capacity was measured as the maximum of m x r, where m is pattern load and r is pattern correlation.

2 α_c was quantified as capacity divided by the number of cells.

3 r_{max} represents maximal pattern correlation during retrieval.

4 Retrieval area is the area enclosed by the half-maximal pattern correlation (r_{max} / 2) contour line in r–m–g_1 plots.

5 For a network with n = 330,000; p = 0.03; b_{valid} = 1, $b_{spurious}$ = 0, i.e. retrieval with original pattern, the information capacity was calculated as 0.08 bits per synapse. This was lower than the information capacity of the Willshaw model with binary learning rule for an autoassociative task (ln 2 / 4 = 0.17 bits synapse^{-1}) (*66*) or the Hopfield model with additive learning rule (1 / (8 ln 2) = 0.18 bits synapse^{-1}) (*64*). However, in our model, (1) capacity was calculated from the product m x r, giving lower values, and (2) the number of active neurons per pattern was not constant, but varied statistically between patterns (which reduces capacity; *67*), (3) finite-size models generally show smaller capacity than infinite-size models (*60*).

6 For a network with n = 330,000; p = 0.03; b_{valid} = 1, $b_{spurious}$ = 0, i.e. retrieval with original pattern, α_c, the pattern-to-neuron ratio, was calculated 0.213. This was higher than the value of a Hopfield model (*11*, *13*), but below the theoretical bound obtained with the Gardner approach (α_c = 2, *68*). Thus, networks based on biological constraints may operate below the theoretical limit.